



Electrical and structural engineering of cobalt selenide nanosheets by Mn modulation for efficient oxygen evolution

Xu Zhao^a, Xingqi Li^a, Yu Yan^a, Yulin Xing^a, Sicheng Lu^a, Liangyong Zhao^a, Shiming Zhou^a, Zhenmeng Peng^{b,*}, Jie Zeng^{a,*}

^a Hefei National Laboratory for Physical Sciences at the Microscale, Key Laboratory of Strongly-Coupled Quantum Matter Physics of Chinese Academy of Sciences,

Department of Chemical Physics, University of Science and Technology of China, Hefei, Anhui, 230026, PR China

^b Department of Chemical and Biomolecular Engineering, The University of Akron, Akron, Ohio, 44325, United States



ARTICLE INFO

Keywords:

Atomic disorder
Electronic structure
Conductivity
Oxygen evolution reaction

ABSTRACT

The efficiency of oxygen evolution reaction (OER) depends critically on the steric and electronic structures of electrocatalysts. Moreover, a high conductivity of electrocatalysts ensures a fast electron transfer and thus plays a significant role in OER. Therefore, the development of efficient electrocatalysts with synergistically engineered structure and conductivity is urgently needed. Here, we present an ingenious design of manganese-modulated cobalt selenide nanosheets with systematically engineered structure and conductivity for efficient OER. Tailored atomic disorder, tuned electronic structure, and optimized electrical conductivity could be simultaneously realized by Mn modulation, leading to effective generation of active sites and promoted OER rate. The resultant (CoMn)Se₂ catalysts exhibited remarkable electrocatalytic OER performance with a 5.8-fold and 10.8-fold higher activity relative to CoSe₂ and state-of-the-art IrO₂. This work provides a comprehensive understanding on origin of high activity of transition metal non-oxide electrocatalysts and enables the rational design of highly efficient electrocatalysts with precisely engineered structural and electrical properties.

1. Introduction

Oxygen evolution reaction (OER), also known as water oxidation, is widely regarded as a critical reaction in renewable energy conversion and storage systems, such as hydrogen fuel generation, photoelectrochemical cells, and rechargeable metal-air batteries [1–3]. Owing to the sluggish kinetics caused by the multistep four-electron redox process, even the state-of-the-art catalysts (e.g., RuO₂ and IrO₂) still require a substantial overpotential, which is the major bottleneck for the energy conversion efficiency [4]. Moreover, the scarcity and high cost of noble metal also limit their commercial application. Accordingly, the development of efficient and cost-effective OER catalysts based on earth-abundant first-row transition metal has been subject of intense research [5–7]. A common approach is to tune the 3d electronic structures by constructing multimetallic nanostructures. Electrochemical studies in combination with density function theory calculations have elucidated that the adsorption energy of OER intermediates could be modulated with the tuned 3d energy levels, leading to an enhanced catalytic activity [8]. For instance, trimetallic WCoFe oxyhydroxides, bimetallic NiFe oxides, and CoFe (oxy)hydroxide have been demonstrated as more efficient OER catalysts [9–11]. Another necessary consideration for

OER catalysts is the electrical conductivity, which plays a significant role in electrocatalysis. A high electrical conductivity ensures a fast electron-transfer process, which could immensely promote the energy conversion efficiency by reducing the overpotential caused by the Schottky barriers at both catalyst-electrolyte and catalyst-electrode interfaces. This has been well demonstrated by the synthesis of metallic nickel carbides, atomically thin cobalt oxyhydroxide, and nickel-doped cobalt selenides for the efficient electrocatalysis [12–14]. Furthermore, nanostructuring to increase surface area is also a known strategy to construct efficient OER catalysts [15]. Nevertheless, comprehensive understanding of these effects is still lacking, making it especially urgent to develop highly efficient OER catalysts systematically.

Recently, various economical transition metal non-oxide species, such as dichalcogenides, carbides, phosphides, and nitrides, have been studied as the promising noble metal-free OER catalysts with high activity [16–19]. For instance, with the lattice strain induced by boron, amorphous cobalt boride has shown high OER activity [20]. Moreover, adjustable band gaps ranging from insulator to metallic state could be achieved with different structures of nickel selenides, leading to promoted OER [21]. Considering the fact that these non-oxides would suffer from electrochemical oxidation to generate actual active species

* Corresponding authors.

E-mail addresses: zpeng@uakron.edu (Z. Peng), zengj@ustc.edu.cn (J. Zeng).

during OER [22], the controlled construction of non-oxides makes it possible to deeply understand the origin of electrocatalytic activity and thereby enable the rational design of high-performance electrocatalysts.

Herein, we develop a simple and facile strategy to fabricate Mn-modulated cobalt selenide nanosheets with systematically engineered structure and conductivity for dramatically accelerated OER process. With the modulation of Mn, the tailored atomic disorder, tuned electronic structure, together with optimized electrical conductivity could be simultaneously achieved in CoMn selenide. The engineered structural and electrical properties led to the effective generation of active species and promoted reaction rate during OER process, in accordance with the high catalytic activity. The overpotential of (CoMn)Se₂ catalysts was 0.27 V at a current density of 10 mA cm⁻², much lower than that of CoSe₂ catalysts and the state-of-the-art IrO₂. Moreover, the (CoMn)Se₂ catalysts showed a current density of 28.08 mA cm⁻² at the overpotential of 0.30 V, which was 5.8-fold and 10.8-fold higher than that of pure CoSe₂ catalysts and state-of-the-art IrO₂.

2. Experimental

2.1. Material preparation

The (Co₄Mn₁)Se₂ nanosheets were fabricated by a typical anion exchange reaction. The typical synthesis was divided into two steps: first, Co₄Mn₁ LDH nanosheets were prepared through the previous methods [23]. In detail, 131 mg of Co(NO₃)₂·6H₂O, 28.2 mg of Mn (NO₃)₂·4H₂O, 76.5 mg of NaNO₃, and 92.6 mg of NH₄F were dissolved into 125 mL N₂-saturated deionized (DI) water. Then 12.5 μL of H₂O₂ was added, followed by the slowly addition of 37.5 mL N₂-saturated NaOH solution (0.08 M). The reaction was maintained at room temperature for 15 h under N₂ atmosphere. Co₄Mn₁ LDH nanosheets were collected and dried under vacuum. Second, 5 mg of LDH nanosheets were dispersed in 12 mL DI water in a vial, followed by adding 7.9 mg of Se and 11.4 mg of NaBH₄ under magnetic stirring. The mixed solution was then transferred into the Teflon-lined autoclave and maintained at 180 °C for 15 h, and the final (Co₄Mn₁)Se₂ nanosheets were obtained. In addition, (Co₂Mn₁)Se₂ and (Co₁Mn₁)Se₂ nanosheets could be prepared by similar selenation process with Co₂Mn₁ LDH and Co₁Mn₁ LDH nanosheets. The Co₂Mn₁ LDH and Co₁Mn₁ LDH nanosheets could be obtained through tuning the ratio of Co and Mn precursors while keeping the total amount of Co and Mn at 0.563 mmol.

2.2. Electrochemical measurements

Electrochemical measurements were performed with a three-electrode system on an IM6 electrochemical workstation (Zahner, Germany). A platinum wire was used as the counter electrode and an Ag/AgCl was used as the reference electrodes. All the potentials were referenced to the reversible hydrogen electrode (RHE) calibration through RHE calibration, and in 1 M KOH, $E_{\text{RHE}} = E_{\text{Ag/AgCl}} + 1.02$ V. For the catalysts and state-of-the-art IrO₂ (99%, Alfa Aesar), approximately 4 mg of the powders was dispersed into 1 mL of a mixture consisted of water, isopropanol alcohol, and 40 μL of 5 wt% Nafion (Aldrich). After ultrasonication for 1 h, suitable microliters of the dispersion was deposited onto the RDE (Pine Instruments) to ensure the loading amount of catalyst to be 200 μg cm⁻². The polarization curves were obtained in an O₂-saturated 1 M KOH electrolyte at a rotation rate of 1600 rpm and a sweep rate of 5 mV/s. The durability tests were carried out in an O₂-saturated 1 M KOH solution by means of the galvanostatic measurement under a current density of 10 mA cm⁻². The overpotential (η) was calculated at a current density of 10 mA cm⁻² according to the following formula: $\eta = E_{\text{RHE}} - 1.23$ V [23–25]. Electrochemical impedance spectroscopy measurement was performed over a frequency range from 1000 kHz to 1 Hz with a sinusoidal voltage amplitude of 5 mV. The total amount of oxygen produced was measured using gas chromatography equipped with a thermal conductivity

detector and Molecular sieve 5 A capillary column. The Faradaic efficiency (FE) was calculated from the total amount of charge (Q) passed through the cell and the total amount of oxygen produced (n_{O_2}). $FE = 4F \times n_{\text{O}_2} / Q$, where F is the Faraday constant.

2.3. Characterizations

TEM images were taken using a Hitachi H-7650 transmission electron microscope at an acceleration voltage of 100 kV. HRTEM, HAADF-STEM images and EDX analyses were collected on a JEOL ARM-200 F field-emission transmission electron microscope operating at 200 kV accelerating voltage. XRD characterization was performed using a Philips X'Pert Pro X-ray diffractometer with a monochromatized Cu K α radiation source and a wavelength of 0.1542 nm. The metal concentrations of Co, Mn, and Se were determined by ICP-AES (Atomscan Advantage, Thermo Jarrell Ash, USA). GBW(E)082102 Mn standard solution (100 μg/mL, NCS Testing Technology Co., Ltd., Beijing), GBW (E)082104 Co standard solution (100 μg/mL, NCS Testing Technology Co., Ltd., Beijing), and GBW(E)080215 Se standard solution (100 μg/mL, National Institute of Metrology, China) were used as standard solutions for ICP-AES analysis. The electrical transport property and Hall coefficient were measured on a Quantum Design Physical Property Measurement System (PPMS).

3. Results and discussion

In a typical synthesis of (CoMn)Se₂ nanosheets, ultrathin CoMn LDH nanosheets were firstly prepared as the starting seeds. The seed took a platelet-like morphology with an average thickness of ca. 3 nm and had a layered double hydroxide structure (Fig. S1). The (CoMn)Se₂ nanosheets were then fabricated via a typical anion exchange reaction between CoMn LDH nanosheets and Se-containing aqueous solution. As shown in Fig. 1A, the transmission electron microscopy (TEM) image of (CoMn)Se₂ nanosheets shows that the ultrathin sheet-like morphology are basically retained after the anion exchange treatment. The high transparency under the electron beams is indicative of the ultrathin nature. The thickness of the sheet-like (CoMn)Se₂ was examined to be 3–4 nm (Fig. S2). The thickness was also demonstrated by atomic force microscopy (Fig. S3). The Co/Mn ratio in the sample was determined to be 4 by inductively coupled plasma-atomic emission spectroscopy (ICP-AES) analysis, as such we denote it as (Co₄Mn₁)Se₂ nanosheets. Fig. 1B shows a high-resolution TEM (HRTEM) image of (Co₄Mn₁)Se₂ nanosheets. The indented lattice spacing of 2.6 Å can be assigned to the (111) planes of CoSe₂ in the orthorhombic phase. The corresponding fast Fourier transform (FFT) pattern (Fig. S4) further confirms the existence of (111) and (220) planes of orthorhombic CoSe₂. Further observation in the magnified high-angle annular dark-field scanning TEM (HAADF-STEM) of (Co₄Mn₁)Se₂ indicates the incorporation of Mn in the matrix (Fig. S5A). The existence of Mn in the lattice was further verified by the EELS measurements from the same area (Fig. S5B). The typical spectrum confirms the co-existence of Co and Mn. The Mn-L₃/L₂ intensity ratio suggests Mn to be in 2+ valence state [26], implying the substitution of Mn in the CoSe₂ structure. Moreover, as marked by the yellow circles, several interconnected nanoparticles with ultra-small sizes and different lattice orientations were observed in the nanosheets, which could create boundaries, defects and dislocations [27]. Scarcely any visible gaps are present at the boundaries, further indicating the good electrical and mechanical contact of the ultra-small nanoparticles. Fig. 1C shows the HRTEM image of the region marked by the box in Fig. 1B. The lattice curvy and distortion were clearly observed, mainly deriving from the mismatch in the degree of Jahn-Teller distortion between Mn-Se and Co-Se coordination octahedra [28]. Such lattice distortion could facilitate a small lattice domain to change orientation due to the lowered energy barrier, leading to the transformation from lattice domains into smaller nanoparticles [27]. In contrast, as demonstrated by the periodic lattice fringes and selected area electron

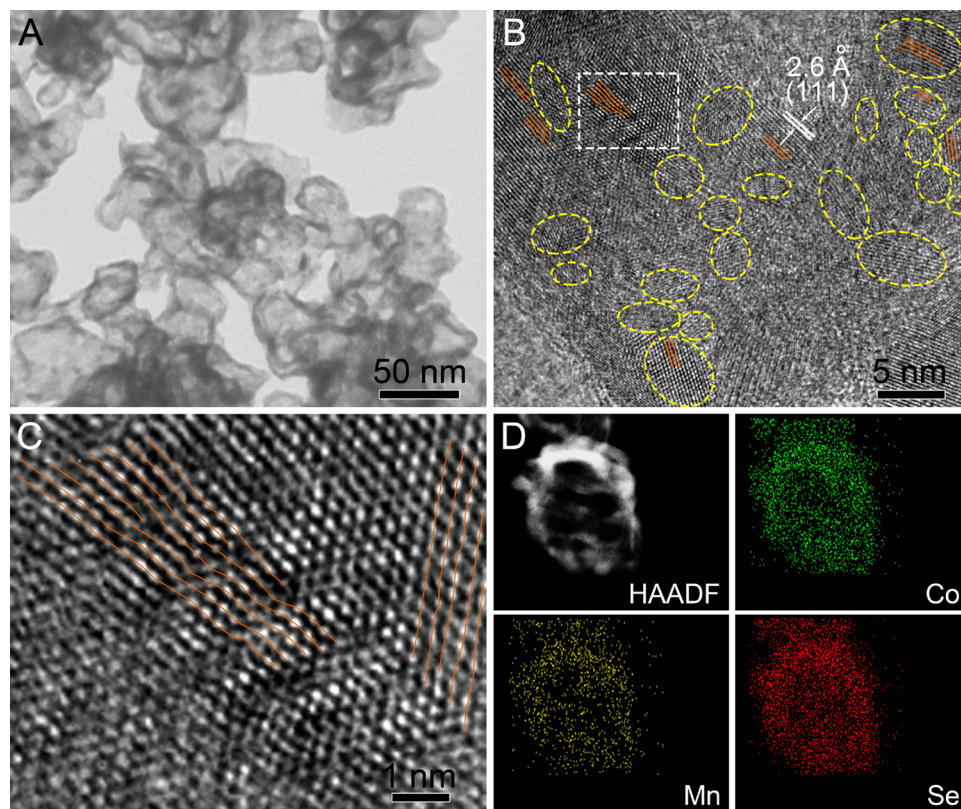


Fig. 1. (A) TEM images of ultrathin (Co_4Mn_1) Se_2 nanosheets. (B) HRTEM image of (Co_4Mn_1) Se_2 nanosheets. The yellow dash lines represent the detached ultra-small nanoparticles. The lattice distortion is marked by the orange lines. (C) Corresponding HRTEM image of the region marked by the white dash lines in B. (D) HAADF-STEM image and STEM-EDX elemental mapping images of Co (green), Mn (yellow) and Se (red) in (Co_4Mn_1) Se_2 nanosheets (For interpretation of the references to colour in this figure legend, the reader is referred to the web version of this article).

diffraction (SAED) pattern, the pure CoSe_2 in Fig. S6 shows the typical monocrystalline nature, further suggesting the varied structure induced by the incorporation of Mn. Fig. 1D shows a high-angle annular dark-field scanning TEM (HAADF-STEM) and corresponding STEM energy-dispersive X-ray (STEM-EDX) elemental mapping images of the (Co_4Mn_1) Se_2 nanosheet. The results uncontestedly demonstrate the homogeneously spatial distribution of Co, Mn, and Se. From the energy dispersive X-ray (EDX) spectrum in Fig. S7, the signal for Co, Mn, and Se can be clearly observed. The absence of O signal further confirms the complete conversion of (CoMn) Se_2 nanosheets from CoMn LDH nanosheets. By simply varying the molar ratios of $\text{Co}(\text{NO}_3)_2$ and $\text{Mn}(\text{NO}_3)_2$ during the synthesis of CoMn LDH (Fig. S8), similar nanosheets with a Co/Mn ratio of 2 and 1 were successfully prepared, which were denoted as (Co_2Mn_1) Se_2 and (Co_1Mn_1) Se_2 nanosheets, respectively (Fig. S9).

The crystalline and electronic structures of (CoMn) Se_2 nanosheets were systematically investigated. The XRD patterns of the (CoMn) Se_2 nanosheets are shown in Fig. 2A. Similar to that of CoSe_2 nanosheets, the result clearly identifies the (CoMn) Se_2 nanosheets with different Co/Mn ratios as an orthorhombic CoSe_2 phase. The disappearance of LDH diffraction peaks indicates the complete conversion during the anion exchange process (Fig. S10). Fig. 2B exhibits the Raman spectra of the (CoMn) Se_2 nanosheets. A typical peak located at 173.5 cm^{-1} was observed for all the (CoMn) Se_2 nanosheets, corresponding to that of the orthorhombic CoSe_2 structure [29]. Moreover, the full-width at half-maximum (FWHM) at 173.5 cm^{-1} was found to increase with the increasing Mn/Co ratio (Fig. S11), further implying the structural disorder caused by the incorporation of Mn [30]. Accordingly, the disorder in (Co_1Mn_1) Se_2 was larger than that in (Co_4Mn_1) Se_2 and CoSe_2 , which was further demonstrated by HRTEM (Fig. S12). Compared to (Co_4Mn_1) Se_2 and CoSe_2 , ultra-small nanoparticles with more lattice curvy and distortion were clearly observed in (Co_1Mn_1) Se_2 , suggesting the increased disorder with the increasing Mn/Co ratio. In addition, XPS analysis was applied to investigate the electronic properties of (CoMn) Se_2 nanosheets. As shown in Fig. 2C, the binding energies of $\text{Co} 2p_{3/2}$ in

(Co_4Mn_1) Se_2 at 779.1 eV and $\text{Co} 2p_{1/2}$ at 794 eV corresponded to Co^{2+} cations in CoSe_2 [31]. The obvious shake-up satellites at the higher energy side of the $\text{Co} 2p$ signal indicate the antibonding orbital between the Co and Se atom [32]. Notably, the gradual shifts of $\text{Co} 2p$ XPS peaks to lower energy were observed with the introduction of Mn, suggesting the modulated electronic structure of Co centers (Table S1). Fig. 2D shows the binding energy of $\text{Mn} 2p_{3/2}$ in (Co_4Mn_1) Se_2 were at 641.1 eV, which can be assigned to Mn^{2+} cations in manganese chalcogenides, confirming the incorporation of Mn in the CoSe_2 nanostructures [33,34]. The valence state is further verified by the Mn 3s XPS analysis, which represents a definite indicator for the Mn valence [35,36]. As shown in Fig. S13, the Mn 3s spectrum splits into a doublet of peaks with a multiplet splitting energy of 6.1 eV, demonstrating the Mn^{2+} states in the (CoMn) Se_2 [37]. Moreover, the Mn 2p peaks in (CoMn) Se_2 show a positive shift to higher binding energy with the increase of Mn contents (Table S1), further indicating the electron transfer between Mn and Co. The highly negative charges in catalysts is believed to optimize the binding energy of OER intermediates and thus facilitate the OER process [38,39]. In addition, the minor broad $\text{Co} 2p_{3/2}$ and $\text{Mn} 2p_{3/2}$ XPS peaks at 781.1 eV and 642.5 eV in Fig. 2C, D were assigned to surface oxides impurities, in accordance with the previous study that the metal selenide's surface is prone to oxidation by air [40–42].

To investigate the influence of the introduced Mn on conductivity, the temperature-dependent resistivity measurements of (CoMn) Se_2 and CoSe_2 nanosheets were carried out. As shown in Fig. 3A, the electrical resistivity of all the (CoMn) Se_2 and CoSe_2 nanosheets increased with temperature ($\rho_0/dT > 0$), implying a typical metallic behavior. Notably, the electrical resistivity of $1.3 \times 10^{-5} \Omega \text{ m}$ for (Co_4Mn_1) Se_2 nanosheets at 300 K was one-magnitude lower than that of $2.16 \times 10^{-4} \Omega \text{ m}$ for CoSe_2 nanosheets, indicating the improved conductivity with the introduction of Mn. Moreover, further increase of Mn in (CoMn) Se_2 led to the increase of electrical resistivity, which could be related to the increased degree of disorder and thus the blocked electron transport [43]. To gain in-depth understanding of the charge transport properties of (CoMn) Se_2 nanosheets, the Hall coefficient (R_H) was measured. As

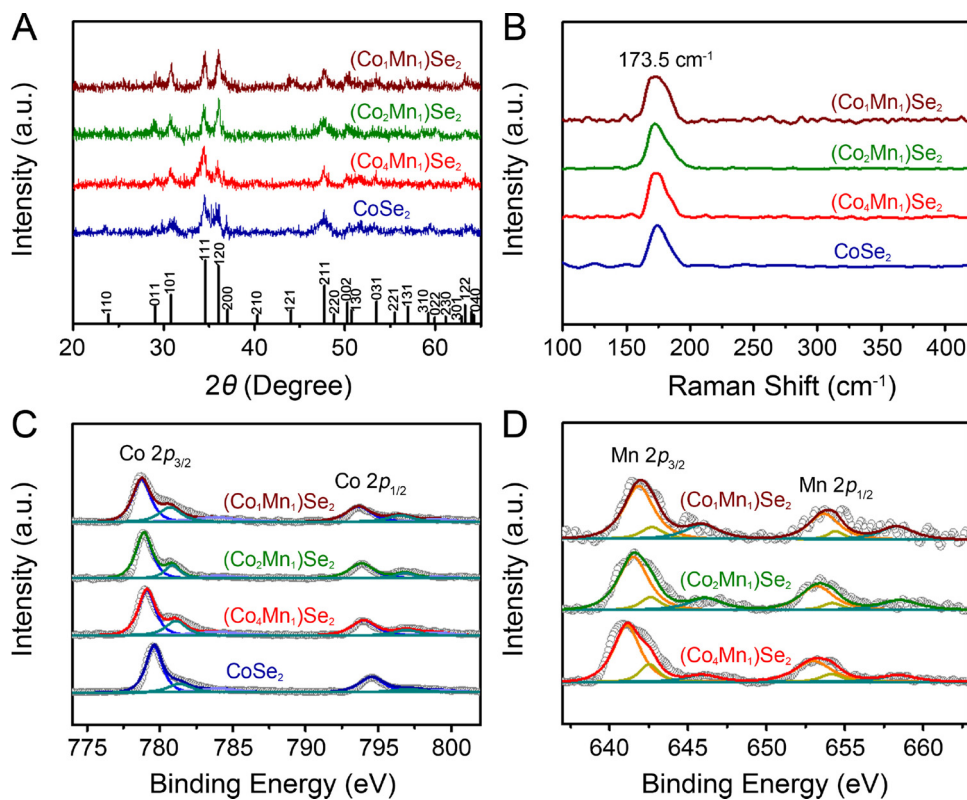


Fig. 2. (A) XRD patterns of $(\text{Co}_1\text{Mn}_1)\text{Se}_2$, $(\text{Co}_2\text{Mn}_1)\text{Se}_2$, $(\text{Co}_3\text{Mn}_1)\text{Se}_2$, and CoSe_2 nanosheets. The standard diffraction peaks of pure CoSe_2 (JCPDS No.01-053-0449) are attached at the bottom for comparison. (B) Raman spectra of $(\text{CoMn})\text{Se}_2$ nanosheets. (C) Co 2p XPS and (D) Mn 2p XPS spectra of $(\text{CoMn})\text{Se}_2$ nanosheets.

shown in Fig. 3B, all the nanosheets show negative R_H at 300 K, indicating that their charge carriers are electrons. The carrier concentration (n) derived from the Hall coefficient for $(\text{Co}_4\text{Mn}_1)\text{Se}_2$ nanosheets shows an increase by 12.6 times at 300 K compared with that of CoSe_2 nanosheets, further indicating the significantly enhanced conductivity of $(\text{Co}_4\text{Mn}_1)\text{Se}_2$ nanosheets. Meanwhile, the $(\text{Co}_1\text{Mn}_1)\text{Se}_2$ only shows an increase by 2.1 times relative to CoSe_2 , confirming the blocked electron transport with the increased disorder by the increase of Mn in $(\text{CoMn})\text{Se}_2$.

The enhanced conductivity and high carrier concentration induced by the incorporation of Mn could promote the charge transfer process that serves as the key step in electrocatalysis, thereby making $(\text{Co}_4\text{Mn}_1)\text{Se}_2$ an ideal candidate for OER. Previous mechanistic studies have revealed that Co^{IV} centers generated in situ through a typical oxidation of Co sites prior to OER act as the actual active species for Co-based catalysts [44]. Specifically, the generation of surface active species could

be facilitated due to the significantly promoted electron transport, leading to more Co^{IV} species generated and consequently promoted OER rate. Moreover, considering that the induced atomic disorder by Mn could also have an impact on the generation of Co^{IV} species owing to the exposure of Co^{II} sites, the electrochemical surface areas (ECSAs), which represent the Co^{II} amounts, were evaluated by capacitance measurements (Fig. S14). As shown in Fig. 4A, the ECSA of $(\text{Co}_4\text{Mn}_1)\text{Se}_2$ was 50.5 m F cm^{-2} , which is 1.2 times higher than that of the CoSe_2 (43.6 m F cm^{-2}). The increased ECSA suggests increased exposure of Co^{II} sites in $(\text{Co}_4\text{Mn}_1)\text{Se}_2$, leading to the generation of more Co^{IV} active species. To gain a deep insight into the surface oxidation to generate actual active species under OER conditions, cyclic voltammograms (CVs) in the potential range of 1.22–1.49 V versus reversible hydrogen electrode (RHE) were employed (Fig. 4B). Relative to that for CoSe_2 , the enlarged pre-OER oxidation peak for $(\text{Co}_4\text{Mn}_1)\text{Se}_2$ at 1.4 V could be assigned to the oxidation of Co^{III} to Co^{IV} [45], indicating the facilitated

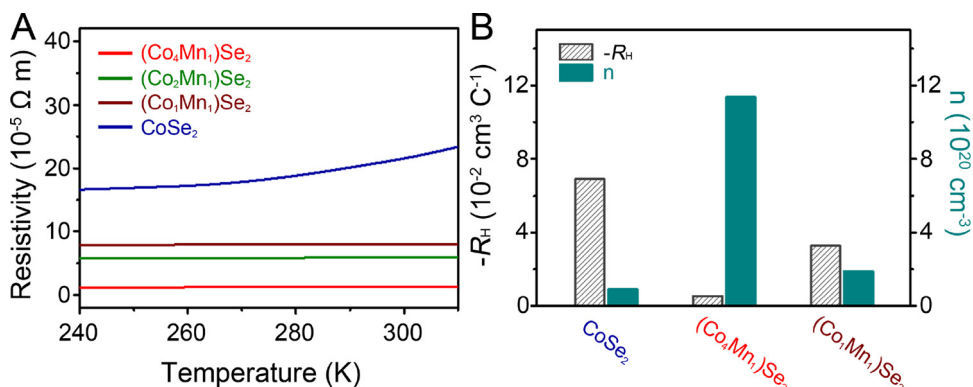


Fig. 3. (A) Temperature-dependent electrical resistivity of $(\text{CoMn})\text{Se}_2$ and CoSe_2 nanosheets. (B) Hall coefficient (R_H) and corresponding carrier concentration (n) of $(\text{CoMn})\text{Se}_2$ and CoSe_2 nanosheets at 300 K.

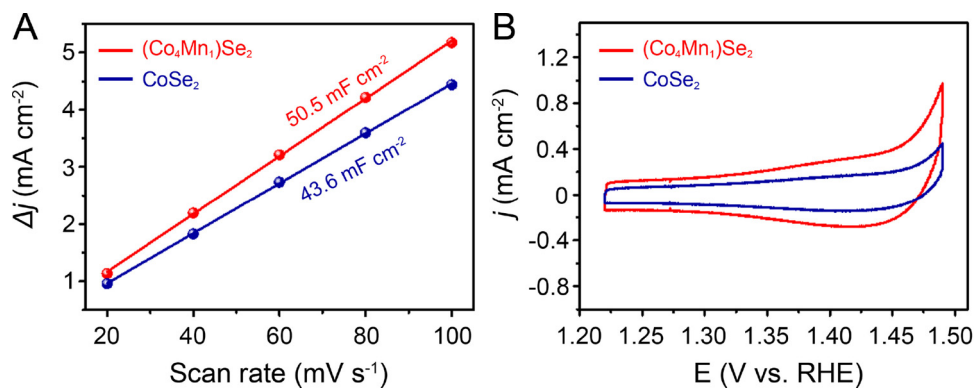


Fig. 4. (A) Charging current density differences ($\Delta j = j_a - j_c$) plotted against scan rates. (B) Cyclic voltammetry curves of CoSe_2 and $(\text{Co}_4\text{Mn}_1)\text{Se}_2$ in 1 M KOH with a scan rates of 5 mV/s.

oxidation of Co sites for more Co^{IV} species. The facilitated oxidation of Co sites in $(\text{Co}_4\text{Mn}_1)\text{Se}_2$ could enhance the electrophilicity of adsorbed oxygen and thus promote the formation of $\text{Co}^{IV}\text{-OOH}$ via nucleophilic attack. The oxidized Co sites could also facilitate the deprotonation of OOH via electron-withdrawing inductive effects to produce O_2 [46].

The electrocatalytic OER properties of $(\text{Co}_4\text{Mn}_1)\text{Se}_2$ were further investigated in an O_2 -saturated 1 M KOH solution in comparison with CoSe_2 and the state-of-the-art IrO_2 . Fig. 5A shows the typical polarization curves recorded through linear sweep voltammetry (LSV) at a sweep rate of 5 mV s⁻¹. The ohmic potential drop (iR) losses were all corrected for electrolyte resistance. Remarkably, the $(\text{Co}_4\text{Mn}_1)\text{Se}_2$ exhibited a much earlier OER onset potential and higher current densities than those of all the tested catalysts. At a current density of 10 mA cm⁻², which represents a metric associated with the solar fuel, the overpotential of $(\text{Co}_4\text{Mn}_1)\text{Se}_2$ was only 274 mV, significantly lower than that of CoSe_2 (317 mV), and state-of-the-art IrO_2 (347 mV), respectively. To directly make a comparison of the electrocatalytic performance of the catalysts, the current densities at a fixed overpotential of 0.30 V were summarized in Fig. 5B. The $(\text{Co}_4\text{Mn}_1)\text{Se}_2$ displayed the

highest electrocatalytic current density of 28.08 mA cm⁻², which was 5.8 and 10.8 times as high as that of CoSe_2 and state-of-the-art IrO_2 catalyst, respectively. Given the proportional relationship between the electrocatalytic reaction current and the oxygen yield, the boosted current density indicates the prominent OER performance of $(\text{Co}_4\text{Mn}_1)\text{Se}_2$. The Faradaic efficiency of $(\text{Co}_4\text{Mn}_1)\text{Se}_2$ was measured to confirm that the current was associated with oxygen evolution. Fig. S15 showed that the amount of oxygen produced at 10 mA cm⁻² increased during continuous electrolysis. By comparing the amount of experimentally quantified oxygen with theoretically calculated oxygen, the Faradaic efficiency during electrocatalytic OER process was calculated to be 96.9%, suggesting that the current is directly related to oxygen evolution. To gain further insight into the oxygen evolution activity, the corresponding Tafel plots were investigated. As shown in Fig. 5C, the Tafel slope for $(\text{Co}_4\text{Mn}_1)\text{Se}_2$ was 39 mV dec^{-1} , relatively lower than that for the CoSe_2 (48 mV dec^{-1}) and state-of-the-art IrO_2 (54 mV dec^{-1}), suggesting the significantly accelerated OER kinetics. Meanwhile, electrochemical impedance spectroscopy (EIS) analysis was performed to gain an in-depth understanding on the OER kinetics of

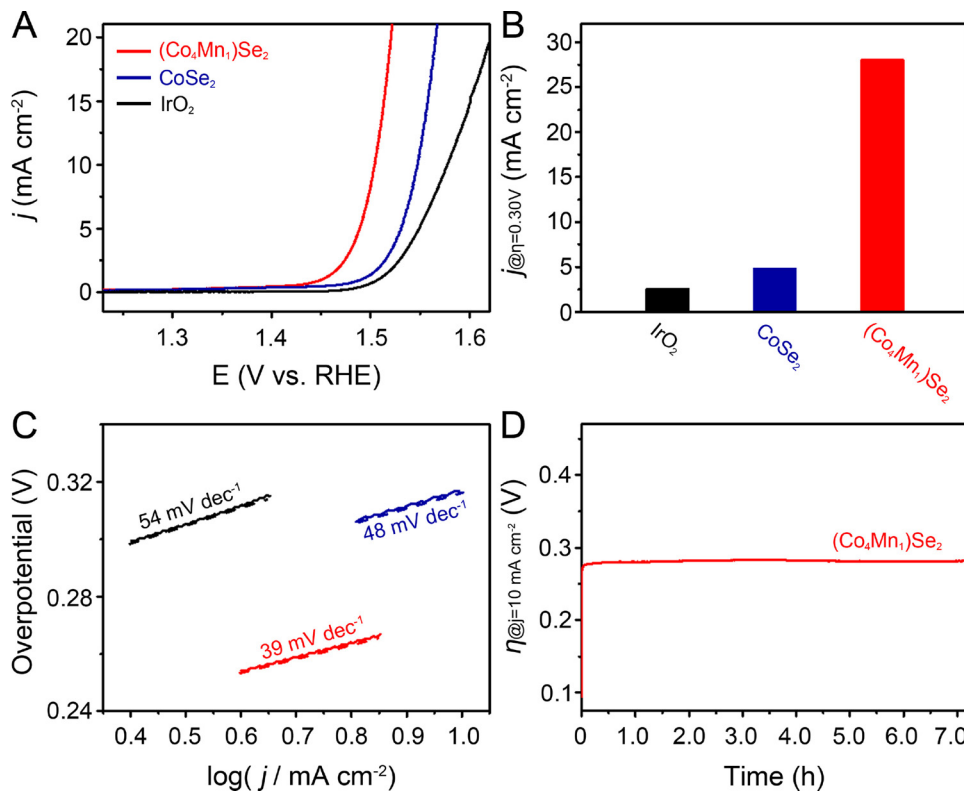


Fig. 5. (A) iR-corrected polarization curves of $(\text{Co}_4\text{Mn}_1)\text{Se}_2$, CoSe_2 and state-of-the-art IrO_2 in O_2 -saturated 1 M KOH solution. (B) Current densities of $(\text{Co}_4\text{Mn}_1)\text{Se}_2$, CoSe_2 and state-of-the-art IrO_2 at the overpotential of 0.30 V. (C) Tafel plots of these catalysts. (D) Galvanostatic measurement of $(\text{Co}_4\text{Mn}_1)\text{Se}_2$ at the current density of 10 mA cm⁻².

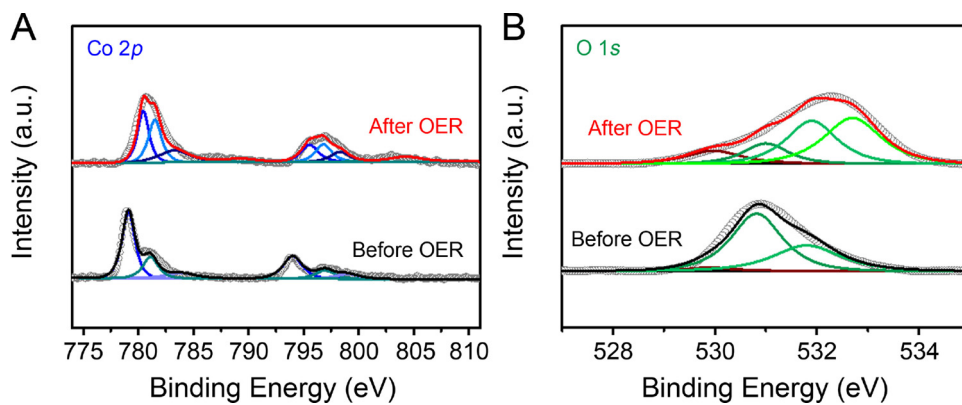


Fig. 6. (A) Co 2p XPS and (D) O 1s XPS spectra of $(\text{Co}_4\text{Mn}_1)\text{Se}_2$ catalysts before and after the durability OER test.

catalysts (Fig. S16). The Nyquist plots showed an obvious semicircle in the high frequency range, which is associated with the charge transfer resistance (R_{ct}). Notably, the $(\text{Co}_4\text{Mn}_1)\text{Se}_2$ exhibited a smaller R_{ct} as compared to CoSe_2 , indicating the improved charge transfer kinetics with the introduction of Mn. The OER activity of $(\text{Co}_4\text{Mn}_1)\text{Se}_2$ is comparable to the performance of many other transition metal non-oxide catalysts (Table S2). Taken together, the enhancement on the catalytic performance for $(\text{Co}_4\text{Mn}_1)\text{Se}_2$ could be attributed to the following factors: (i) increased exposure of Co sites, (ii) tailored electronic structure, and (iii) facilitated electron transport, leading to more $\text{Co}^{\text{III/IV}}$ active species and promoted OER rate. Furthermore, to investigate composition-dependent OER activities, $(\text{CoMn})\text{Se}_2$ catalysts with different Co/Mn ratios (1, 2, and 4) were also measured. As shown in Fig. S17A, the OER activity increased monotonically, with Co/Mn ratios rising from 1 to 4. The $(\text{Co}_4\text{Mn}_1)\text{Se}_2$ displayed higher current densities than those of all the tested catalysts. The specific activities of $(\text{CoMn})\text{Se}_2$ catalysts were compared on the basis of active surface areas (Fig. S17B). The $(\text{Co}_4\text{Mn}_1)\text{Se}_2$ showed a current density of 0.07 mA cm^{-2} at 1.5 V vs. RHE, which was 2.2, 3.3 and 5.0 times higher than that of $(\text{Co}_2\text{Mn}_1)\text{Se}_2$, $(\text{Co}_1\text{Mn}_1)\text{Se}_2$ and CoSe_2 , further suggesting the largely enhanced intrinsic activity.

In addition, galvanostatic measurement in O_2 -saturated 1 M KOH solution at a constant current density of 10 mA cm^{-2} was carried out to access the OER durability of $(\text{Co}_4\text{Mn}_1)\text{Se}_2$ catalysts. As shown in Fig. 5D, the variation of overpotential observed after 7-h testing could be neglected, indicating the high durability for OER. Moreover, the TEM image of $(\text{Co}_4\text{Mn}_1)\text{Se}_2$ catalysts showed that the sheet-like morphology was retained after the durability test (Fig. S18A). To further investigate the surface structure of $(\text{Co}_4\text{Mn}_1)\text{Se}_2$ under OER conditions, XPS analysis was carried out after the durability test. The binding energies of Co $2p_{3/2}$ at 780.5 eV, 781.5 eV, 783.3 eV and 789.3 eV in $(\text{Co}_4\text{Mn}_1)\text{Se}_2$ after the durability test corresponded to Co^{3+} cations, indicating the surface oxidation of $(\text{Co}_4\text{Mn}_1)\text{Se}_2$ (Fig. 6A). The O 1s XPS spectra in Fig. 6B showed four contributions at 529.9 eV, 531 eV, 531.9 eV, and 532.7 eV, which could be attributed to the metal-oxygen bonds, oxygen in $-\text{OH}$ groups, surface-absorbed SeO_2 , and absorbed water, respectively [14,47]. Notably, the intensity of the peak attributed to Co-O bonds at 529.9 eV increased enormously after OER, in accordance with the surface oxidation of $(\text{Co}_4\text{Mn}_1)\text{Se}_2$ under OER conditions. The corresponding HRTEM image in Fig. S18B further confirms the surface oxidation of $(\text{Co}_4\text{Mn}_1)\text{Se}_2$ with the formation of amorphous structure, which was also demonstrated by XRD characterization (Fig. S19).

4. Conclusion

In conclusion, we demonstrate an ingenious design of Mn-modulated cobalt selenide nanosheets with precisely engineered structure and conductivity for highly efficient water oxidation. In detail, with the

modulation of Mn, tailored atomic disorder, tuned electronic structure, together with optimized electrical conductivity could be achieved in $(\text{Co}_4\text{Mn}_1)\text{Se}_2$. Moreover, the evolution of catalysts for the generation of actual active species was also monitored during OER, making it accessible to understand the origin of OER activity. This work presents a comprehensive understanding on the origin of high catalytic activity of transition metal non-oxide electrocatalysts and a convenient strategy to develop advanced electrocatalysts based on synergistically engineering structural and electrical properties for energy-related technologies.

Acknowledgements

This work was supported by Collaborative Innovation Center of Suzhou Nano Science and Technology, MOST of China (2014CB932700), NSFC (21573206), Key Research Program of Frontier Sciences of the CAS (QYZDB-SSW-SLH017), Anhui Provincial Key Scientific and Technological Project (1704a0902013), Major Program of Development Foundation of Hefei Center for Physical Science and Technology (2017FXZY002), and Fundamental Research Funds for the Central Universities. This work was partially carried out at the USTC Center for Micro and Nanoscale Research and Fabrication.

Appendix A. Supplementary data

Supplementary material related to this article can be found, in the online version, at doi: <https://doi.org/10.1016/j.apcath.2018.05.054>.

References

- [1] A. Grimaud, O.D. -Morales, B.H. Han, W.T. Hong, Y.-L. Lee, L. Giordano, K.A. Stoerzinger, M.T.M. Koper, Y. Shao-Horn, Activating lattice oxygen redox reactions in metal oxides to catalyse oxygen evolution, *Nat. Chem.* 9 (2017) 457–465.
- [2] J.H. Yang, J.K. Cooper, F.M. Toma, K.A. Walczak, M. Favaro, J.W. Beeman, L.H. Hess, C. Wang, C.H. Zhu, S. Gul, J. Yano, C. Kisielowski, A. Schwartzberg, I.D. Sharp, A multifunctional biphasic water splitting catalyst tailored for integration with high-performance semiconductor photoanodes, *Nat. Mater.* 16 (2017) 335–341.
- [3] L.S. Zhang, J.J. Lu, S.B. Yin, L. Luo, S.Y. Jing, A. Brouzgou, J.H. Chen, P.K. Shen, P. Tsiaikaras, One-pot synthesized boron-doped RhFe alloy with enhanced catalytic performance for hydrogen evolution reaction, *Appl. Catal. B: Environ.* 230 (2018) 58–64.
- [4] Y. Jiao, Y. Zheng, M. Jaroniec, S.Z. Qiao, Design of electrocatalysts for oxygen- and hydrogen-involving energy conversion reactions, *Chem. Soc. Rev.* 44 (2015) 2060–2086.
- [5] L. Han, S.J. Dong, E.K. Wang, Transition-metal (Co, Ni, and Fe)-based electrocatalysts for the water oxidation reaction, *Adv. Mater.* 28 (2016) 9266–9291.
- [6] J.F. Ping, Y.X. Wang, Q.P. Lu, B. Chen, J.Z. Chen, Y. Huang, Q.L. Ma, C.L. Tan, J. Yang, X.H. Cao, Z.J. Wang, J. Wu, Y.B. Ying, H. Zhang, Self-assembly of single-layer CoAl-layered double hydroxide nanosheets on 3D graphene network used as highly efficient electrocatalyst for oxygen evolution reaction, *Adv. Mater.* 28 (2016) 7640–7645.
- [7] M. Kim, S. Kim, D. Song, S. Oh, K.J. Chang, E. Cho, Promotion of electrochemical oxygen evolution reaction by chemical coupling of cobalt to molybdenum carbide, *Appl. Catal. B: Environ.* 227 (2018) 340–348.
- [8] B. Zhang, X.L. Zheng, O. Voznyy, R. Comin, M. Bajdich, M.G. -Melchor, L.L. Han,

[8] J.X. Xu, M. Liu, L.R. Zheng, F.P.G.D. Arquer, G.T. Dinh, F.J. Fan, M.J. Yuan, E. Yassitepe, N. Chen, T. Regier, P.F. Liu, Y.H. Li, P.D. Luna, A. Jammohamed, H.L.L. Xin, H.G. Yang, A. Vojvodic, E.H. Sargent, Homogeneously dispersed multmetal oxygen-evolving catalysts, *Science* 352 (2016) 333–337.

[9] Y.C. Pi, Q. Shao, P.T. Wang, F. Lv, S.J. Guo, J. Guo, X.Q. Huang, Trimetallic oxyhydroxide coralloids for efficient oxygen evolution electrocatalysis, *Angew. Chem. Int. Ed.* 56 (2017) 4502–4506.

[10] X.Y. Lu, C. Zhao, Electrodeposition of hierarchically structured three-dimensional nickel–iron electrodes for efficient oxygen evolution at high current densities, *Nat. Commun.* 6 (2015) 6616.

[11] M.S. Burke, M.G. Kast, L. Trotochaud, A.M. Smith, S.W. Boettcher, Cobalt–iron (oxy)hydroxide oxygen evolution electrocatalysts: the role of structure and composition on activity, stability, and mechanism, *J. Am. Chem. Soc.* 137 (2015) 3638–3648.

[12] K. Xu, H. Ding, H.F. Lv, P.Z. Chen, X.L. Lu, H. Cheng, T.P. Zhou, S. Liu, X.J. Wu, C.Z. Wu, Y. Xie, Dual electrical-behavior regulation on electrocatalysts realizing enhanced electrochemical water oxidation, *Adv. Mater.* 28 (2016) 3326–3332.

[13] J.H. Huang, J.T. Chen, T. Yao, J.F. He, S. Jiang, Z.H. Sun, Q.H. Liu, W.R. Cheng, F.C. Hu, Y. Jiang, Z.Y. Pan, S.Q. Wei, CoOOH nanosheets with high mass activity for water oxidation, *Angew. Chem. Int. Ed.* 54 (2015) 8722–8727.

[14] C. Xia, Q. Jiang, C. Zhao, M.N. Hedhili, H.N. Alshareef, Selenide-based electrocatalysts and scaffolds for water oxidation applications, *Adv. Mater.* 28 (2016) 77–85.

[15] Z.W. Seh, J. Kibsgaard, C.F. Dickens, I. Chorkendorff, J.K. Norskov, T.F. Jaramillo, Combining theory and experiment in electrocatalysis: insights into materials design, *Science* 355 (2017) eaad4998.

[16] B.Y. Guan, L. Yu, X.W. Lou, General synthesis of multishell mixed-metal oxyphosphide particles with enhanced electrocatalytic activity in the oxygen evolution reaction, *Angew. Chem. Int. Ed.* 56 (2017) 2386–2389.

[17] P.W. Cai, J.H. Huang, J.X. Chen, Z.H. Wei, Oxygen-containing amorphous cobalt sulfide porous nanocubes as high-activity electrocatalysts for the oxygen evolution reaction in an alkaline/neutral medium, *Angew. Chem. Int. Ed.* 56 (2017) 4858–4861.

[18] J.H. Wang, W. Cui, Q. Liu, Z.C. Xing, A.M. Asiri, X.P. Sun, Recent progress in cobalt-based heterogeneous catalysts for electrochemical water splitting, *Adv. Mater.* 28 (2016) 215–230.

[19] M.R. Gao, Y.R. Zheng, J. Jiang, S.H. Yu, Pyrite-type nanomaterials for advanced electrocatalysis, *Acc. Chem. Res.* 50 (2017) 2194–2204.

[20] J. Masa, P. Weide, D. Peeters, I. Sinev, W. Xia, Z.Y. Sun, C. Somsen, M. Muhler, W. Schuhmann, Amorphous cobalt boride (Co₂B) as a highly efficient nonprecious catalyst for electrochemical water splitting: oxygen and hydrogen evolution, *Adv. Energy Mater.* 6 (2016) 1502313.

[21] K. Xu, H. Ding, H.F. Lv, S. Tao, P.Z. Chen, X.J. Wu, W.S. Chu, C.Z. Wu, Y. Xie, Understanding structure-dependent catalytic performance of nickel selenides for electrochemical water oxidation, *ACS. Catal.* 7 (2017) 310–315.

[22] Y.Q. Zhang, B. Ouyang, J. Xu, G.C. Jia, S. Chen, R.S. Rawat, H.J. Fan, Rapid synthesis of cobalt nitride nanowires: highly efficient and low-cost catalysts for oxygen evolution, *Angew. Chem. Int. Ed.* 55 (2016) 8670–8674.

[23] F. Song, X.L. Hu, Ultrathin cobalt–manganese layered double hydroxide is an efficient oxygen evolution catalyst, *J. Am. Chem. Soc.* 136 (2014) 16481–16484.

[24] C.C.L. McCrory, S. Jung, J.C. Peters, T.F. Jaramillo, Benchmarking heterogeneous electrocatalysts for the oxygen evolution reaction, *J. Am. Chem. Soc.* 135 (2013) 16977–16987.

[25] L. Han, X.Y. Yu, X.W. Lou, Formation of Prussian-blue-analog nanocages via a direct etching method and their Conversion into Ni–Co-mixed oxide for enhanced oxygen oxygen evolution, *Adv. Mater.* 28 (2016) 4601–4605.

[26] Z.L. Wang, J.S. Yin, Y.D. Jiang, EELS analysis of cation valence states and oxygen vacancies in magnetic oxides, *Micro* 31 (2000) 571–580.

[27] H.T. Wang, H.W. Lee, Y. Deng, Z.Y. Lu, P.C. Hsu, Y.Y. Liu, D.C. Lin, Y. Cui, Bifunctional non-noble metal oxide nanoparticle electrocatalysts through lithium-induced conversion for overall water splitting, *Nat. Commun.* 6 (2015) 7261.

[28] Y.W. Liu, X.M. Hua, C. Xiao, T.F. Zhou, P.C. Huang, Z.P. Guo, B.C. Pan, Y. Xie, Heterogeneous spin states in ultrathin nanosheets induce subtle lattice distortion to trigger efficient hydrogen evolution, *J. Am. Chem. Soc.* 138 (2016) 5087–5092.

[29] P.Z. Chen, K. Xu, S. Tao, T.P. Zhou, Y. Tong, H. Ding, L.D. Zhang, W.S. Chu, C.Z. Wu, Y. Xie, Phase-transformation engineering in cobalt diselenide realizing enhanced catalytic activity for hydrogen evolution in an alkaline medium, *Adv. Mater.* 28 (2016) 7527–7532.

[30] K. Samanta, P. Bhattacharya, R.S. Katiyar, W. Iwamoto, P.G. Pagliuso, C. Rettori, Raman scattering studies in dilute magnetic semiconductor Zn_{1-x}Co_xO, *Phys. Rev. B* 73 (2006) 245213.

[31] W.W. Zhao, C. Zhang, F.Y. Geng, S.F. Zhuo, B. Zhang, Nanoporous hollow transition metal chalcogenide nanosheets synthesized via the anion-exchange reaction of metal hydroxides with chalcogenide ions, *ACS Nano* 10 (2014) 10909–10919.

[32] J. Yang, G.H. Cheng, J.H. Zeng, S.H. Yu, X.M. Liu, Y.T. Qian, Shape control and characterization of transition metal diselenides MSE₂ (M = Ni, Co, Fe) prepared by a solvothermal-reduction process, *Chem. Mater.* 13 (2001) 848–853.

[33] A.B. Mandale, S. Badrinarayanan, S.K. Date, A.P.B. Sinha, Photoelectron-spectroscopic study of nickel, manganese and cobalt selenides, *J. Electron Spectrosc. Relat. Phenom.* 33 (1984) 61–72.

[34] H. Van Der Heide, R. Hemmel, C.F. Van Bruggen, C. Haas, X-ray photoelectron spectra of 3d transition metal pyrites, *J. Solid State Chem.* 33 (1980) 17–25.

[35] E. Beyreuther, S. Grafstrom, L.M. Eng, C. Thiele, K. Dorr, XPS investigation of Mn valence in lanthanum manganite thin films under variation of oxygen content, *Phys. Rev. B* 73 (2006) 155425.

[36] T. Gao, F. Krumeich, R. Nesper, H. Fjellvag, P. Norby, Microstructures, surface properties, and topotactic transitions of manganite nanorods, *Inorg. Chem.* 48 (2009) 6242–6250.

[37] T. Gao, P. Norby, F. Krumeich, H. Okamoto, R. Nesper, H. Fjellvag, Synthesis and properties of layered-structured Mn₅O₈nanorods, *J. Phys. Chem. C* 114 (2010) 922–928.

[38] S. Zhao, R.X. Jin, H. Abroshan, C.J. Zeng, H. Zhang, S.D. House, E. Gottlieb, H.J. Kim, J.C. Yang, R.C. Jin, Gold nanoclusters promote electrocatalytic water oxidation at the nanocluster/CoSe₂interface, *J. Am. Chem. Soc.* 139 (2017) 1077–1080.

[39] M.R. Gao, X. Cao, Q. Gao, Y.F. Xu, Y.R. Zheng, J. Jiang, S.H. Yu, Nitrogen-doped graphene supported CoSe₂nanobel composite catalyst for efficient water oxidation, *ACS Nano* 8 (2014) 3970–3978.

[40] B.J. Tan, K.J. Klabunde, P.M.A. Sherwood, XPS studies of solvated metal atom dispersed catalysts. Evidence for layered cobalt–manganese particles on alumina and silica, *J. Am. Chem. Soc.* 113 (1991) 855–861.

[41] K.J. Zhang, P.X. Han, L. Gu, L.X. Zhang, Z.H. Liu, Q.S. Kong, C.J. Zhang, S.M. Dong, Z.Y. Zhang, J.H. Yao, H.X. Xu, G.L. Cui, L.Q. Chen, Synthesis of nitrogen-doped MnO/graphene nanosheets hybrid material for lithium ion batteries, *ACS Appl. Mater. Interfaces* 4 (2012) 658–664.

[42] X. Xu, F. Song, X.L. Hu, A nickel iron diselenide-derived efficient oxygen-evolution catalyst, *Nat. Commun.* 7 (2016) 12324.

[43] J.F. Xie, J.J. Zhang, S. Li, F. Grote, X.D. Zhang, H. Zhang, R.X. Wang, Y. Lei, B.C. Pan, Y. Xie, Controllable disorder engineering in oxygen-incorporated MoS₂ultrathin nanosheets for efficient hydrogen evolution, *J. Am. Chem. Soc.* 135 (2013) 17881–17888.

[44] Z.B. Zhang, W.C. Sheng, Y.S. Yan, Synthesis of monodispere Au@Co₃O₄ core-shell nanocrystals and their enhanced catalytic activity for oxygen evolution reaction, *Adv. Mater.* 26 (2014) 3950–3955.

[45] Y.C. Liu, J.A. Koza, J.A. Switzer, Conversion of electrodeposited Co(OH)₂ to CoOOH and Co₃O₄, and comparison of their catalytic activity for the oxygen evolution reaction, *Electrochim. Acta* 140 (2014) 359–365.

[46] B.S. Yeo, A.T. Bell, Enhanced activity of gold-supported cobalt oxide for the electrochemical evolution of oxygen, *J. Am. Chem. Soc.* 133 (2011) 5587–5593.

[47] J. Yang, H.W. Liu, W.N. Martens, R.L. Frost, Synthesis and characterization of cobalt hydroxide, cobalt oxyhydroxide, and cobalt oxide nanodiscs, *J. Phys. Chem. C* 114 (2010) 111–119.